Magnetic Resonance Imaging 60 (2019) 68–75

Contents lists available at ScienceDirect

Magnetic Resonance Imaging

journal homepage: www.elsevier.com/locate/mri

Original contribution

Differentiating platinum coated brachytherapy seeds and gold fiducial markers with varying off-resonant frequency offsets

Evan McNabb[a], Raimond Wong[b,c,d], Michael D. Noseworthy[a,e,f,g,*]

[a] McMaster School of Biomedical Engineering, McMaster University, Hamilton, Ontario, Canada
[b] Juravinski Cancer Centre, Hamilton, Ontario, Canada
[c] Department of Oncology, McMaster University, Hamilton, Ontario, Canada
[d] Department of Medicine, McMaster University, Hamilton, Ontario, Canada
[e] Department of Electrical and Computer Engineering, McMaster University, Hamilton, Ontario, Canada
[f] Department of Radiology, McMaster University, Hamilton, Ontario, Canada
[g] Imaging Research Centre, St. Joseph's Healthcare, Hamilton, Ontario, Canada

ARTICLE INFO

Keywords:
Co-RASOR
Contrast
Gold fiducial marker
Brachytherapy
Platinum
Visualization

ABSTRACT

Purpose: To develop an off-resonant frequency filtered method to selectively differentiate between implanted gold fiducial markers and platinum coated brachytherapy seeds.

Materials and methods: The magnetic susceptibilities for gold fiducial markers and brachytherapy seeds differ in magnitude and also in their signs, resulting in B_0-field inhomogeneity patterns with opposite main lobes. A pulse sequence used to localize brachytherapy seeds with positive contrast, centre-out radial sampling with off-resonance reception (co-RASOR), was used to reconstruct images with a range of off-resonant frequency offsets. The proposed method utilizes two frequency filters to selectively reconstruct maximum intensity projections through band-pass regions where each seed has its maximal localized hyperintensity. Seeds were simulated and then placed in gel and tissue phantoms to validate the technique using orthogonal 2D slices with seeds both parallel and perpendicular to the B_0-field.

Results: Dual-plane 2D co-RASOR sequences were reconstructed off-resonance with applied frequency filters to create two projections displaying each seed, which were then colour-coded to negative and positive frequencies. Phantom validation showed that each seed contains its maximal CNR in opposing frequency regions as predicted. Local maxima can also appear in both negative and positive frequency regions. The relative difference between the signal of each seed and these local maxima ranged from 1.19 to 3.73, and an image threshold was determined in all cases. Tissue validation showed the technique differentiates seeds correctly and is limited by the hyperintensity patterns observed in the co-RASOR method.

Conclusions: Dual-plane co-RASOR offers sub-millimetre positive contrast from implanted seeds that contain unique off-resonant frequency maxima, which frequency filters can selectively differentiate.

1. Introduction

Magnetic resonance (MR) imaging has seen continued use for management of prostate image guided radiation therapy (IGRT) due to superior soft tissue contrast compared to computed tomography (CT), thus leading to reduced clinical target volumes and interobserver variability [1,2]. The dosimetric and geometric accuracy of MR-only based treatment procedures have been recently reported with acceptable differences in doses < 2% [3–6]. MR adoption has been aided through the use of MR simulators that use flat-top benches in therapy position, procedures to standardize immobilization, and dosimetric calculations from MR-only data [7–9].

Two current issues in MR-only workflows are (i) identification of implanted gold fiducial markers (GFMs) with positive contrast, and (ii) differentiating GFMs from brachytherapy seeds in patients undergoing radiosurgical external beam radiation therapy for regional recurrent disease. The latter still requires a small FOV CT scan that adds to pre-treatment acquisition time in sites attempting MR-only workflows [10]. Identifying paramagnetic SPIOs with positive contrast has been reviewed for a number of 3D sequences [11–14], susceptibility

* Corresponding author at: Department of Electrical and Computer Engineering, McMaster University, Engineering Technology Building, ETB-406, 1280 Main St. West, Hamilton, Ontario L8S 4K1, Canada.
E-mail address: nosewor@mcmaster.ca (M.D. Noseworthy).

https://doi.org/10.1016/j.mri.2019.04.005
Received 26 April 2018; Received in revised form 14 March 2019; Accepted 4 April 2019

approaches [15], template matching algorithms [16–18] and machine learning from multi-parametric MR [19], all taking advantage of signal void artifacts to build models and improve detection rates of GFMs over standard negative contrast imaging. However, differentiating GFMs and therapy seeds directly with the same pulse sequence remains insufficient. An MR pulse sequence, developed for visualizing low-dose rate brachytherapy seeds with positive contrast, centre-out radial sampling with off-resonance reception (co-RASOR), has shown promise by radially rewinding hyperintense signal pileups towards the centre artifact by reconstructing offline using a projection of off-resonant frequency offsets [20,21]. Furthermore, it can be implemented as a fast dual-plane 2D acquisition improving imaging times over 3D approaches [22].

Using the co-RASOR sequence, as opposed to other susceptibility techniques, creates approximately symmetric signal hyperintensities around the seeds, and a single parameter, an applied frequency offset, radially shifts these inward or outward depending on the magnetic susceptibility. Here we propose to differentiate the two seeds based on their differing magnetic susceptibilities, with gold being diamagnetic ($\chi_m < 0$) and the platinum layer of the brachytherapy seed being paramagnetic ($\chi_m > 0$). This alters B_0-magnetic field inhomogeneity patterns observed using the co-RASOR signal model as the signs of ΔB_z are opposite for each seed for similar orientations. Where one seeds hyperintensities are shifted inward, a seed of opposite magnetic susceptibility would be smeared outward and eventually thresholded away. Each seed can then be reconstructed using a smaller subset of off-resonant frequency ranges and individually identified with positive contrast from a dual-plane sequence.

2. Materials and methods

The reconstruction modifications to the co-RASOR sequence with the off-resonant frequency regions used for calculating maximum intensity projections (MIPs) are shown in Fig. 1. The in-plane B_0-field inhomogeneity from two spherical field perturbers create hyperintense signal pileups that can be reconstructed off-resonance for a range of offsets. The existing co-RASOR reconstructions use iterative techniques, applying a range of off-resonant reconstructions, followed by a maximum intensity threshold over the frequency offsets, to find the offset that maximizes the image domain intensity. The image is then reconstructed at this optimal offset. By removing this frequency from the set and repeating the process a final superimposed image of all thresholded seeds are found. The proposed method utilizes the fact that signal pileups are maximal for alternating signs, and are centred at distinct frequency offsets at smaller bandwidths (light and dark shaded regions in Fig. 1 denoted as Δf_1 and Δf_2 respectively). A MIP over a smaller frequency range can be used to mask each perturber that can be superimposed and colour-coded to visualize each individually.

All MR images were acquired using a 3 T GE Discovery MR750 (General Electric Healthcare, Milwaukee, WI) with maximum gradients of 50 mT/m and 200 T/m/s slew rate, using GE's 32-channel head coil. The gold seeds were diamagnetic GFM (IZI Medical Products, MD, USA) with diameter 1.2 mm and length 3.0 mm. The brachytherapy seeds were paramagnetic ^{125}I LDR (DraxImage Model LS-1, Quebec, Canada) with diameter 0.8 mm and length 4.3 mm, containing a 10% platinum outer layer. Image reconstruction for co-RASOR datasets were performed using a non-uniform Fast Fourier Transform (NUFFT) [23] implemented in MATLAB R2014b (The Mathworks Inc., Natick, MA). Two fully sampled pulse sequences were used to identify the seeds: 3D bSSFP and dual-plane co-RASOR (described below for each experiment) without the use of acceleration.

To selectively differentiate GFMs and LDR brachytherapy seeds, we first demonstrated the proposed method in a numerical simulation using cylindrical objects with magnetic susceptibility differences $\Delta\chi_m = -25$ ppm and $\Delta\chi_m = +50$ ppm to approximately match those of GFMs and brachytherapy seeds respectively [24]. The differences in size and field inhomogeneity are shown in Fig. 2a–b. The simulated phantom was sampled onto centre-out k-space (FOV = 16 cm; 14 slices, thickness = 4 mm, 256^2 matrix, 804 uniformly spaced spokes). The GFM and brachytherapy seeds were visually identified as colour-coded masks (Fig. 2c–d) in the following manner. First, reconstructions, of k-space off-resonant by a range of frequency offsets δf_i (-1 kHz to $+1$ kHz in step sizes of 50 Hz) were performed, resulting in a series of *i*-images. The on-resonant image is subtracted to suppress the bulk background signals. Next, a frequency filter was used to isolate the hyperintense signals from each seed since positive contrast can be isolated to unique positive and negative δf_i offsets. The positive and negative frequency filters have the following form:

$$H_N = u(-\delta f_i + \alpha_N)$$
$$H_P = u(\delta f_i - \alpha_P) \quad (1)$$

where α_P and α_N were set to $+450$ Hz and -500 Hz, respectively and u (t) represents the Heaviside step function. These values were chosen experimentally to preserve the largest off-resonant signal maxima, and suppress both the opposite half of the frequency offsets, and values closer to 0 Hz containing background signals. In both planes, localized positive contrast was maximal for the GFM at negative offsets and for the brachytherapy seed at positive offsets, depicted by arrows in Fig. 2e. Finally, after the filter was applied element-wise to the *i*-images, a MIP followed by an image threshold (60%) was applied to visualize each seed as a negative-filtered image and positive-filtered image. The frequency filters are further shown in Fig. 3. The positive and negative filters, followed by a MIP through the off-resonant frequencies are shown for the axial and coronal planes (Fig. 3a,b), and with a 60% threshold to create individual positive contrast of each seed (Fig. 3c,d), which were used for the colour overlays. To remove spurious hyperintensities along air/tissue interfaces, we created a binary mask of both seeds that was applied to the final images for improved specificity. This binary mask was used in our previous work [25], and utilizes the locations of the signal pileups from both imaging planes, as they share a Right-Left axis.

A 3D bSSFP (TE/TR = 1.3/3.5 ms, bandwidth = 976 Hz/pixel, FOV = 12.0 cm^2, 256 × 256, thickness = 1.0 mm, NEX = 2, $\alpha = 20°$) was used to image the entire volume of interest with T2/T1 contrast to clearly display both seeds with negative contrast with respect to background. The 2D dual-plane co-RASOR sequences (Minimum TE, TE/TR = 2.7/100 ms; FOV = 16.0 cm; thickness = 3.0 mm; 256 readout points, 804 uniformly distributed spokes; bandwidth = 244 Hz/pixel) were scanned in the axial and coronal planes. Both planes were selected to intersect and cover the entire expected region of field inhomogeneity from each seed. Slice selection was performed with a one-cycle SINC pulse (transmit bandwidth = 4.4 kHz; duration = 900 μs) in order to minimize echo time and intravoxel dephasing. All co-RASOR data was acquired on-resonance, with linear phase ramps modulating each k-space spoke by δf prior to image reconstruction in 50 Hz increments.

The two seeds were first placed in a 3% agar phantom lying co-planar parallel to the B_0-field. The 3D bSSFP was scanned coronally with an extent of 8.4 cm and a scan time of 3:59. Dual-plane co-RASOR scans were performed with 5 axial slices covering 15 mm in the SI-direction and 6 coronal slices covering 18 mm in the AP-direction, for a scan time of 1:22 for each volume. Off-resonant reconstructions of both planes were performed over the range of -1300 to $+1300$ Hz and the off-resonant frequency filters were applied with α_P and α_N set to $+/-$ 350 Hz, followed by MIPs through the positive and negative band-pass regions to visualize each seed individually. Contrast-to-noise (CNR) curves were calculated by two repeated scans using the average signal from a 2 × 2 pixel region encompassing the centre of each seed, as determined by the bSSFP and on-resonant co-RASOR scans, and subtracted from the signal of a 3 mm shell surrounding this area. The signal difference was divided by the standard deviation of the noise within the

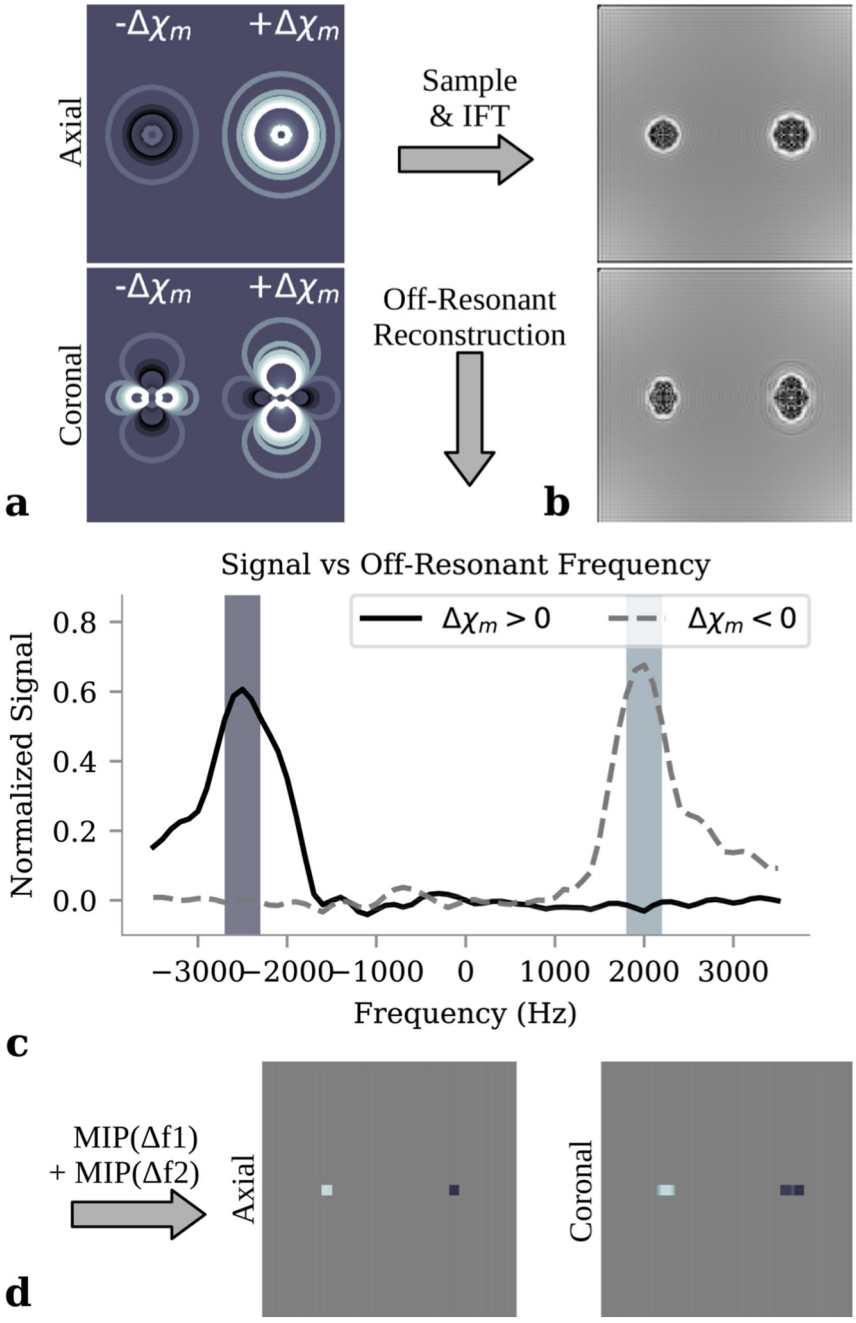

Fig. 1. Field inhomogeneity with contour lines in two imaging planes of spherical perturbers with negative and positive susceptibility (a) and the subsequent co-RASOR image highlighting signal pileups symmetrically around the perturbers (b). The centre pixel intensities in the axial plane are shown as a function of off-resonant frequency offset, where the signal maxima are located (light and dark shaded bandwidths) at distinct negative and positive offsets (c). Performing a MIP over each of these bandwidths can visualize each perturber separately (light and dark overlays) at the geometric centre of the perturbers in each plane (d).

3 mm shell to obtain the CNR for each seed as a function of off-resonant frequency. The noise is derived from the difference of two successive scans [26]. The scans were repeated with seeds lying perpendicular to the B_0-field as this changes the field inhomogeneity pattern for each seed.

Finally, two seeds were injected into porcine muscle tissue, obtained from a local food market, with a needle and guiding wire and placed in a container with external fiducial markers. The porcine tissue was imaged with seeds parallel to B_0 using a coronal bSSFP (20.0 cm × 9.6 cm, $\alpha = 10^{\circ}$) for a scan time of 4:06. Dual-plane co-RASOR images were acquired undersampled (402 spokes, $R = 2$) in the axial and coronal directions covering 18 and 15 mm respectively for a scan time of 0:43 each. The porcine sample was then rotated with the seeds lying perpendicular to B_0 and the study was repeated, with 19 axial slices covering 57 mm in the SI-direction and 6 coronal slices covering 18 mm in the AP-direction, for a scan time of 1:24 and 0:43 respectively. The frequency filters and reconstruction ranges used were identical to the phantom experiment above.

3. Results

Images from the bSSFP, on-resonant 2D co-RASOR, and the frequency filtered masks in a phantom containing a LDR brachytherapy seed and GFM are shown in Fig. 4. Orthogonal views are shown for each sequence, although the axial view for the bSSFP has been reformatted from a coronal acquisition. The frequency filtered images were

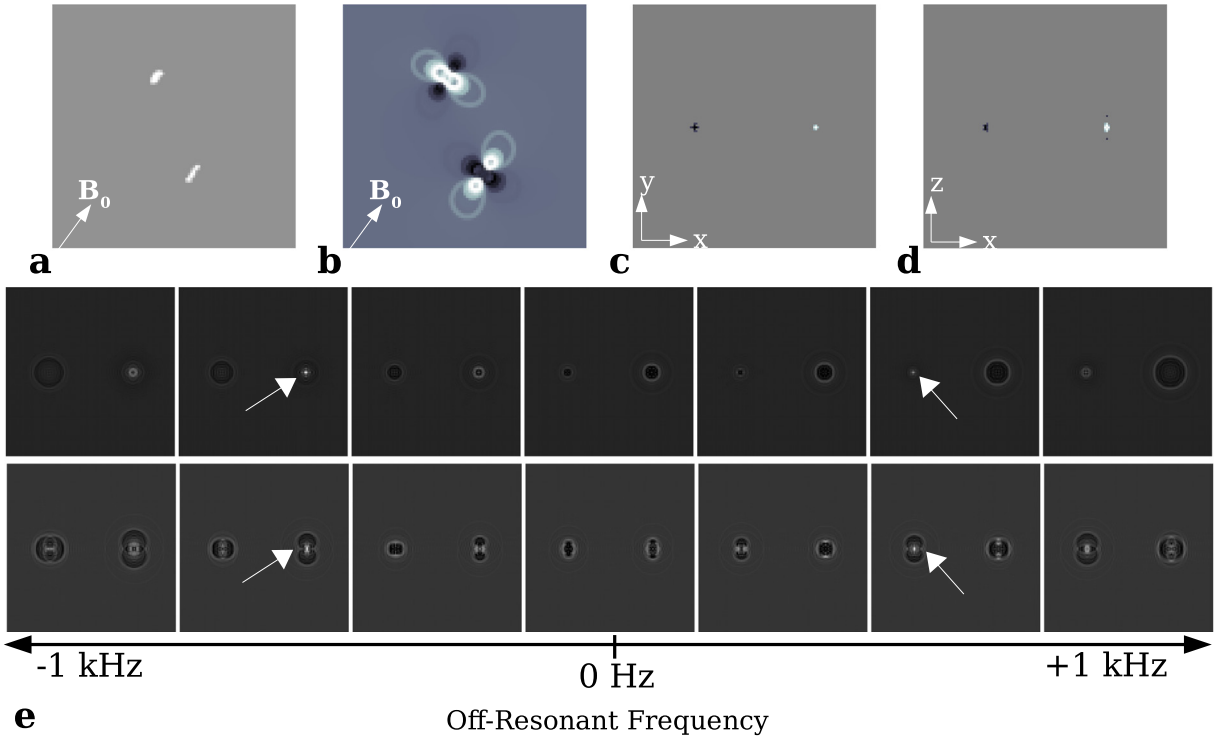

Fig. 2. Viewpoint projections of a simulated LDR brachytherapy seed and a gold fiducial marker (a) and their respective field inhomogeneity patterns displaying opposite patterns (b) lying parallel to the B0-field. Reconstructed dual-plane co-RASOR images using both a positive and negative off-resonant frequency filter displays each seed individually (light and dark overlays) in the axial (c) and coronal (d) planes. The opposite field inhomogeneity patterns cause the hyperintense signals of each seed (white arrows) to be maximal at negative and positive frequency positions (e).

obtained by applying the negative and positive frequency filters over the range of slices displaying field inhomogeneity patterns from the seeds, followed by maximum intensity projections and global image threshold. Comparing bSSFP and on-resonant co-RASOR, the bSSFP displays non-specific negative contrast and severe banding artifacts when formatted in the coronal plane. Likewise, negative contrast was seen in the on-resonant 2D co-RASOR images, however the hyperintense signal pileups were evident around each marker (curved arrow LDR; straight arrow GFM) which can be radially rewinded with negative and positive frequency filters to mask each individual seed.

The contrast mechanism for masking seeds based on opposite magnetic susceptibility is further explored in Fig. 5, where CNR curves are displayed from the cross-section of each seed (Fig. 5a,b), and the long-axis area (Fig. 5c,d) parallel and perpendicular to the B_0-field. Each CNR maximum occurs in the frequency band-pass region highlighted by the colour-coded shaded areas. MIPs can then be taken across the band-pass range in the series of off-resonant images. Smaller, local maxima were also observed for each curve on the opposite off-resonant frequency region as the side lobes of the inhomogeneity match the opposite seed's main lobe. The relative CNR differences between the brachytherapy seed's maximum and local maxima in the displayed frequency regions were 1.64, 2.19, 2.72, and 1.23 for each of the seed orientations, respectively. Similarly, the relative differences between the GFM's signal maximum and local maxima were 2.09, 1.94, 3.73,

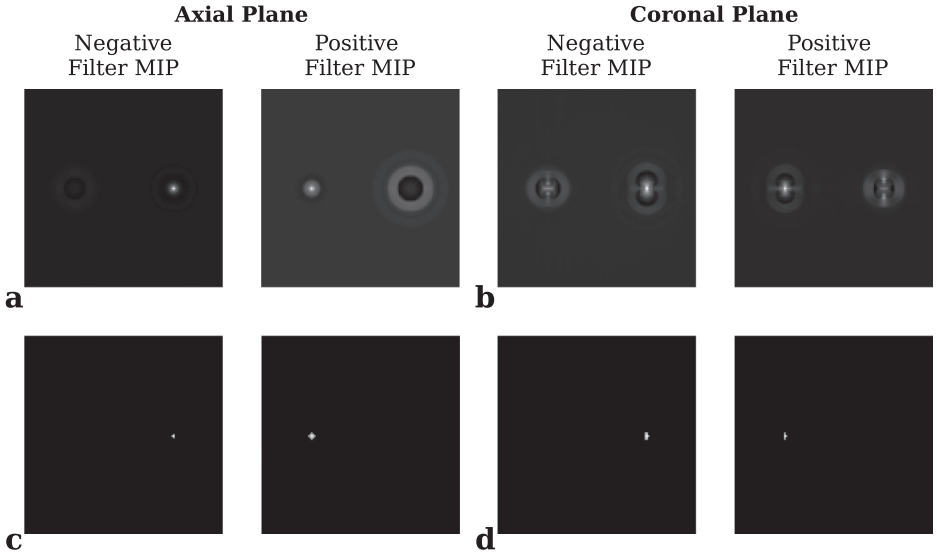

Fig. 3. Maximum intensity projections through the off-resonant frequencies with the applied negative and positive filters from the numerical simulations in the axial (a) and coronal (b) planes. Positive contrast is seen surrounding each seed using a single filter. A 50% threshold was applied in both planes (c–d) to suppress background signals further.

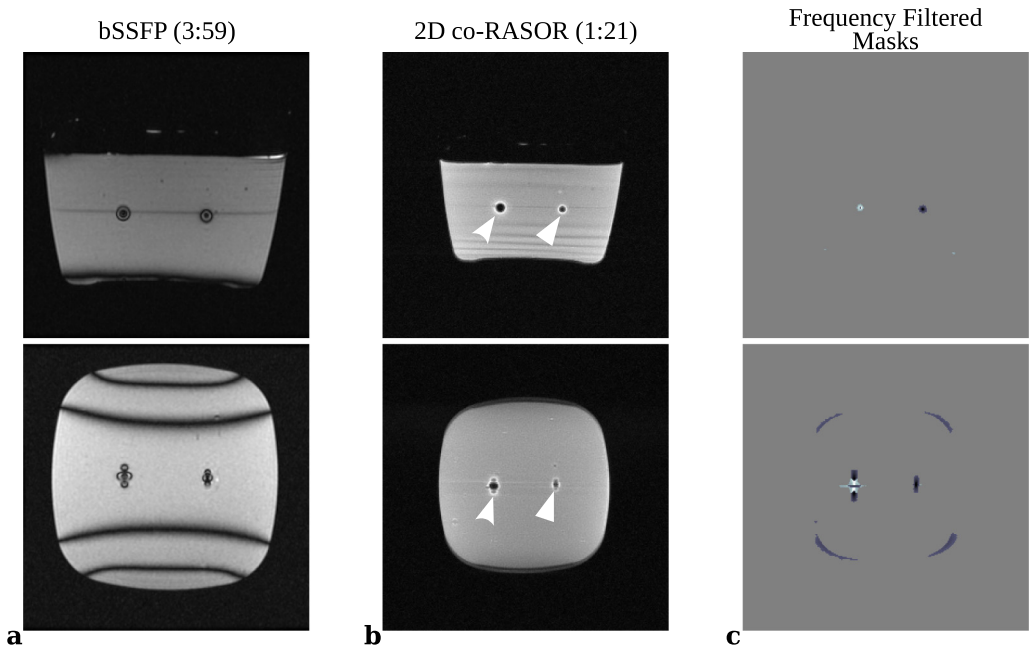

Fig. 4. Comparisons of negative contrast bSSFP sequence (a), on-resonance 2D co-RASOR displaying hyperintensities (b), and the proposed frequency filtered masks that highlight a LDR brachytherapy seed and gold fiducial marker respectively (c). The acquired planes are axial (top-row) and coronal (bottom-row) with each seed parallel to the B_0 field. The 3D bSSFP produces higher global SNR compared to 2D co-RASOR, but identifying unique seeds is difficult because the size of the signal void depends both on the size of the seed and its magnetic susceptibility. However, frequency filtered co-RASOR can produce superimposed masks of each seed.

and 1.19.

Images from the porcine sample are displayed in Fig. 6 including the bSSFP for negative contrast, and frequency filtered masks that are colour-coded and overlaid onto on-resonant co-RASOR from the slices containing the seeds. The colour-coding scheme shows the LDR brachytherapy seed in red and GFM in yellow. The bottom insets display zoomed colour-coded masks from negative and positive frequency filtered MIPs. However, in the coronal view perpendicular to the B_0-field, the colour-coding contrast is inverted. This plane displayed hyperintensities with the opposite filter relative to the three other cases. The bSSFP images also have negative contrast depending on acquired plane and orientation with appreciable contrast reduction and banding when imaged perpendicular to the B_0-field.

4. Discussion

Dual-plane co-RASOR can be used to selectively differentiate seeds with opposite polarity in their magnetic susceptibilities as their signal pileups rewind to the centre of each seed at off-resonant frequencies with opposite signs, which can be filtered with two band-pass filters

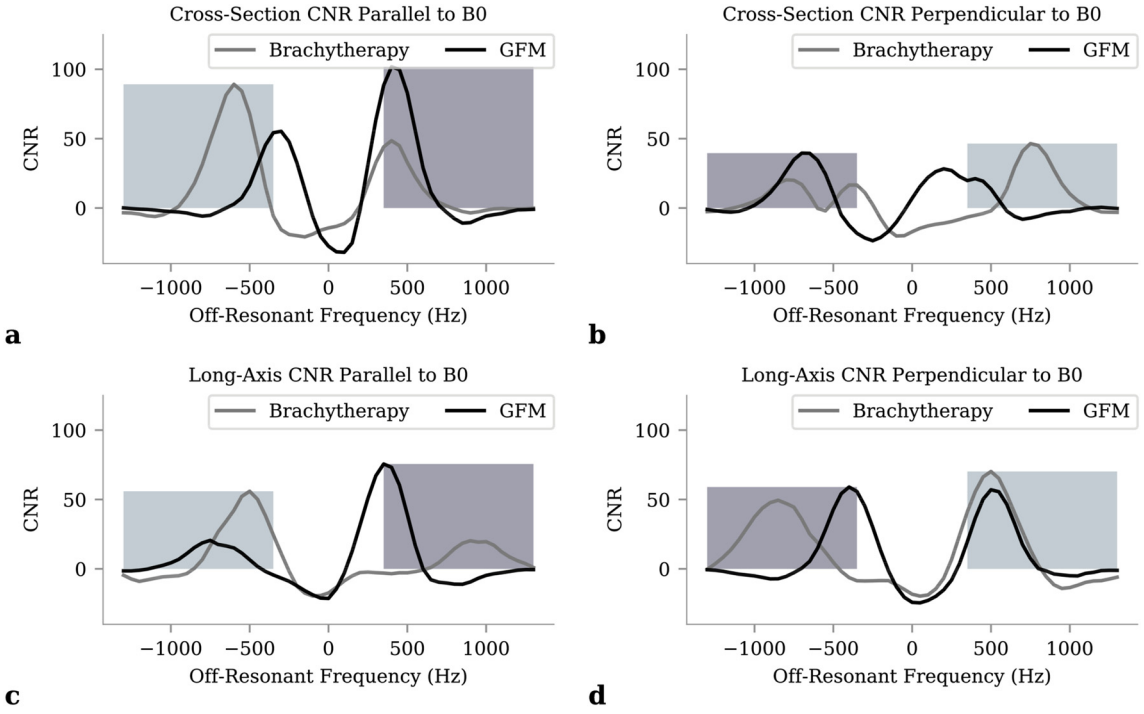

Fig. 5. Contrast-to-noise curves centred on the cross-sectional area of the LDR brachytherapy seed (gray curve) and GFM (black curve) parallel (a) and perpendicular (b) to the B_0 field. Similarly, CNR curves centred on the long-axis of each seed both parallel (c) and perpendicular (d) to the B_0 field are displayed. The shaded regions correspond to the band-pass region of the applied negative and positive off-resonant filters, and their heights match the global maxima of each CNR curve, highlighting that the signal maxima are localized to their unique offset frequencies. Local maxima from the opposite seed were observable, however smaller in all cases.

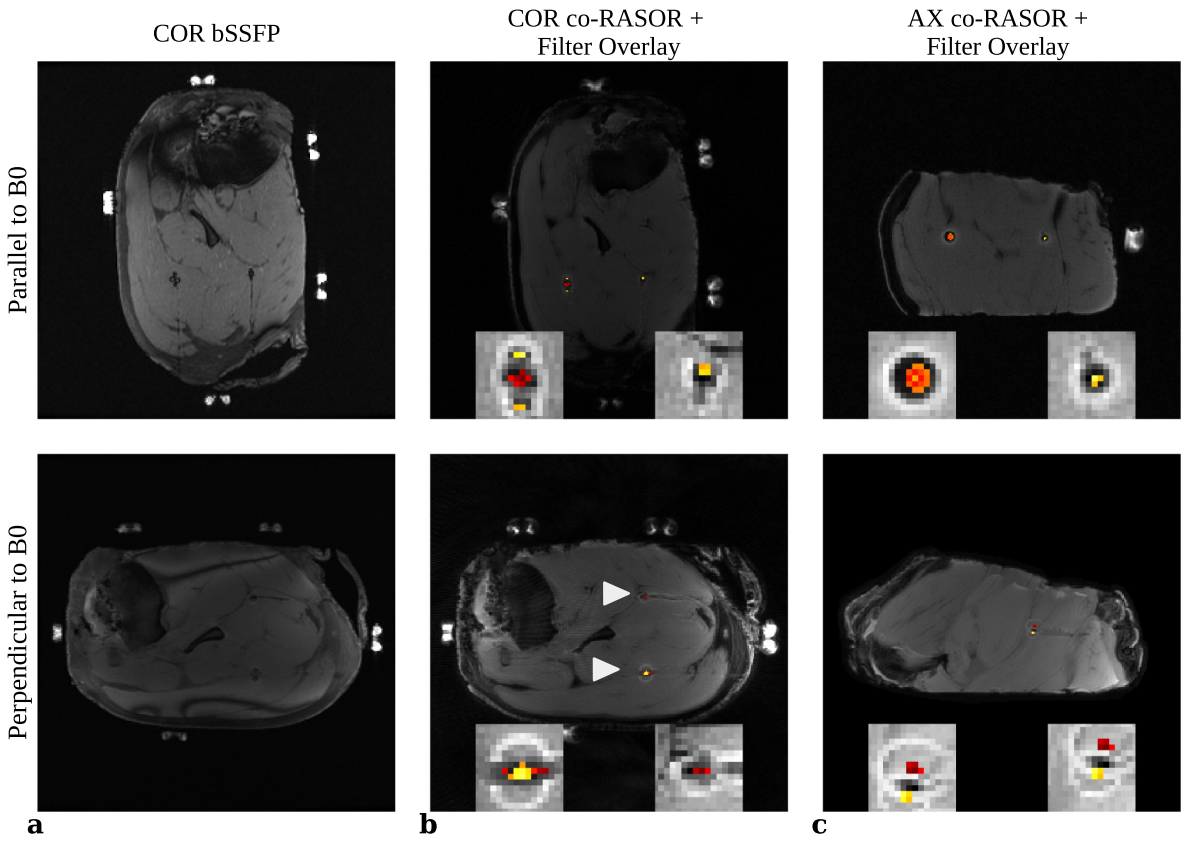

Fig. 6. Comparisons of a negative contrast bSSFP sequence (a) with on-resonance 2D co-RASOR images with frequency filtered overlays in the coronal (b) and axial (c) directions. Both seeds are shown lying parallel (top-row) and perpendicular (bottom-row) to the B_0 field, as the phantom was rotated. The colour overlays represent the negative frequency MIP (red) and positive frequency MIP (yellow). The positive contrast is inverted for the GFM and the LDR brachytherapy seed in the coronal plane when perpendicular to B_0 (highlighted by the white arrow). (For interpretation of the references to colour in this figure legend, the reader is referred to the web version of this article.)

described above. The multiple off-resonant filtered images can be combined into a single MIP, containing one seed, and colour-coded to visualize each seed individually. We have demonstrated this technique in phantoms containing two seeds with seed-specific positive contrast and compared that to a fully sampled 3D bSSFP sequence, which identified the seed locations with non-specific negative contrast. Additionally, this technique displays better temporal resolution by sacrificing total imaging depth by viewing only the in-plane location of the seeds. Quicker volume coverage was achieved by using thicker slices (> 3 mm), as the localization is performed from orthogonal in-plane locations.

Previously, de Leeuw and colleagues [21] used 3D co-RASOR and iterative techniques to visualize LDR brachytherapy seeds and needles. The main difference between our approach and this previous work is prior application of filters to selectively group frequency regions for a particular seed, based on prior knowledge of the seed composition. As seen in phantom validation CNR curves (Fig. 5), the CNR from each seed, in all orientations, is maximal in opposing frequency regions, and there is a large enough contrast difference in each frequency region to separate the seeds. For example, while imaging the cross-section (Fig. 5a), the brachytherapy seed has global maxima at -600 Hz, but also displays a local maximum at 400 Hz, the same frequency where the GFM contrast is maximal. The difference between CNR is important, as the CNR of the GFM at this frequency is 102, while the brachytherapy seed is 48, and a threshold can highlight the signals from just the GFM. This behaviour is seen for each orientation and imaging plane where the relative differences between global and local maxima in the same shaded band-pass region are between 1.19 and 3.73. The worst cases correspond to the long-axis perpendicular to B_0 (Fig. 5d), where the relative difference is not as strong and makes thresholding more difficult. These plots also demonstrate that a single cut-off frequency, experimentally determined, is sufficient to isolate the unique frequency ranges.

The applied technique was also performed on a porcine sample where at least one imaging plane correctly differentiated the seeds (Fig. 6). When the seeds were imaged parallel to the B_0-field, the surrounding hyperintensities closely matched the symmetric patterns observed in our simulation and phantom studies. We previously demonstrated 2D localization displays plane-dependent hyperintensities about the seeds, either point-symmetric or as a dipole pattern [27], and can be reconstructed to positive contrast points. Thus, both planes (top-row Fig. 6) are able to reconstruct the seeds at opposing frequency regions. Similarly, even when the seeds are perpendicular to the B_0-field (bottom-row Fig. 6), the axial plane also displays the point-symmetric pattern that reconstruct to opposing frequency regions. Furthermore, the orientations cannot be directly compared to each other as the LDR signal maxima occurs in the positive frequency MIP (white arrow Fig. 6), whereas in all other scans it occurs using a negative frequency MIP. However, if one plane can correctly identify unique seeds, they can be differentiated as the second plane is used for localization purposes along the orthogonal direction.

While the additional filters to the co-RASOR reconstruction are easy to implement, several limitations should be considered. The SNR in the 2D dual-plane sequence is lower than its 3D version and contrast is reduced by increased echo-time. Also, there are number of acquisition parameters that may influence the degree of signal pileups, such as transmit/receive bandwidth, slice thickness, FOV, and resolution. We attempted to maximize the available transmit bandwidth to incorporate

more off-resonance spins, however the remaining parameters still control the pixel shifts of the hyperintensities. Further experimentation to address how these parameters are selected and weighted would be beneficial to ensure pileups rewind to the small areas with high CNR. Our choice of magnetic susceptibilities were determined from previous experimental data for gold, platinum, and titanium susceptibilities relative to tissue [15,24,28]. It's difficult to directly measure the total susceptibility of brachytherapy seeds as they made up of multiple materials. We used the results of Dong et al. that estimated the total magnetic susceptibility difference of titanium brachytherapy seeds to be +50 ppm, which was used in our simulations [15]. This value for the paramagnetic brachytherapy seed is less than susceptibility difference of pure platinum or pure titanium, and is consistent with the fact that the brachytherapy seeds used here contained a 10% platinum coating. Our simulations take into account the objects field inhomogeneity and shape, so a 3.0 mm cylinder with uniform field inhomogeneity would cause similar effects as a 3.0 mm gold fiducial. In practice, air/tissue interfaces are more difficult to simulate due to irregular shapes and non-stationary susceptibility differences. We observed air bubbles in the phantom in Fig. 4, as well as an air interface along the needle path left behind in the porcine tissue in Fig. 6, though they did not negatively influence the co-RASOR MIPs. We only anticipate issues with air/tissue interfaces if they are directly within the organ of interest and they contain the same flat edges that cause symmetric signal pileups in the image domain.

The choice of frequency cut-off also needs to be experimentally determined. The choice of frequency offsets can be estimated by the bandwidth per pixel and expected pixel shift. Simulated and acquired images used same acquisition window, and FOVs ranging from 12 to 16 cm. Absolute cut-off frequencies were between 350 and 500 Hz. Differences between these cut-offs may be that the true susceptibility differences do not match the simulations, or that the signal pileups are blurred over adjacent voxels.

Positive contrast resolution and determining the number of possible seeds that can be visualized was not addressed in this study as the seeds are separated by > 3 cm in both phantoms. Clinically, a separation of > 1 cm is desired to avoid clustering, though positive contrast resolution is an ongoing area of research. Currently, determining the maximum number of detectable seeds and their spacing has been explored previously, which should be approximately 1 cm for the dual-plane co-RASOR sequence [25]. This study restricted itself to viewing just one GFM and brachytherapy seed. This study did not compare against titanium surgical clips, however it may be useful in the future to address more clinical situations. Finally, each seed has a main lobe in its field inhomogeneity, but also contains two half-lobes of opposite sign (Fig. 2b) which would reconstruct in the opposing frequency region. This study included signals from these opposing regions which were successfully thresholded away (Fig. 5), however it necessitates the inclusion of a threshold that requires manual tuning.

The bSSFP images with negative contrast were also able to depict the seed locations (Figs. 4,6). Banding artifacts observed can be quite severe (Figs. 4a, 6a), and depend on the acquisition plane. Our study used a smaller range in the SI-direction than compared to a routine prostate exam, and increased the minimum TR for the bSSFP sequence. Banding could be reduced in the future through larger FOVs or phase cycling. Our study chose the acquisition plane with the lowest acquisition time for each case. This 3D sequence was chosen as a comparison because of its sensitivity to T2/T1 changes [29] in the vicinity of the seeds to create sharper negative contrast. Furthermore, the use of high readout bandwidth attempts to limit the in-plane distortions caused by the seeds.

The proposed method acquires the same data used in conventional co-RASOR imaging, where the frequency filters were applied only during reconstruction. The primary objective of the sequence is to localize seeds with positive contrast, which has previously been explored. To apply this approach clinically, dual-plane co-RASOR can be positioned over the signal voids in orthogonal directions prior to any contrast enhancement studies. Care should be taken to position the planes so they intersect the field inhomogeneity areas created by all of the seeds, as localization is required in two orthogonal planes for three-dimensional locations. The area surrounding the seeds must also contain signal, as these create signal pileups in the vicinity for positive contrast. For example, a seed too close to bone (Fig. 6) may not create the necessary signal pileups to rewind to positive contrast. The number of slices should cover the full range of expected seed locations. The increase in scan time can be limited by increasing the slice thickness upwards to 5.0 mm as needed. The use of frequency information from each seed would then occur after localization in three dimensions due to the increased reconstruction time of so many off-resonant frequencies. Once accurate localization has been performed, the best imaging plane that displays symmetric hyperintensities about each seed can be used to colour-code the masks if their signal maxima occur in opposite frequency regions. The acquisition time for our sequence was less than the 3D bSSFP by imaging thicker (3.0 mm) orthogonal slices and limiting the through-plane extent to contain the seeds. This approach clearly aids in differentiating LDR brachytherapy seeds from GFMs.

5. Conclusions

We demonstrated that specific positive contrast is possible between paramagnetic LDR brachytherapy seeds and gold fiducial markers with a single co-RASOR sequence. The proposed method uses frequency offset filters, where positive contrast maxima from each seed occur in frequency regions with opposite signs as their magnetic susceptibilities differ in sign. The proposed frequency filtering can create MIPs that display each seed separately, which can then be overlaid and colour-coded to differentiate implanted seeds. This is clinically useful in situations where MR-only simulation is used for combined brachytherapy and external beam radiation therapy to potentially avoid CT-based differentiation.

Acknowledgements

This project was supported by an Ontario Graduate Scholarship (OGS) to EM. The authors also thank the financial contributions by Robert Dunsmore that made the work possible.

References

[1] Dubois DF, Prestidge BR, Hotchkiss LA, Prete JJ, Bice WS. Intraobserver and interobserver variability of MR imaging- and CT-derived prostate volumes after transperineal interstitial permanent prostate brachytherapy. Radiology 1998;207:785–9. https://doi.org/10.1148/radiology.207.3.9609905.

[2] Villeirs GM, Van Vaerenbergh K, Vakaet L, Bral S, Claus F, De Neve WJ, et al. Interobserver delineation variation using CT versus combined CT + MRI in intensity–modulated radiotherapy for prostate Cancer. Strahlentherapie Und Onkol 2005;181:424–30. https://doi.org/10.1007/s00066-005-1383-x.

[3] Tyagi N, Fontenla S, Zhang J, Cloutier M, Kadbi M, Mechalakos J, et al. Dosimetric and workflow evaluation of first commercial synthetic CT software for clinical use in pelvis. Phys Med Biol 2017;62:2961–75. https://doi.org/10.1088/1361-6560/aa5452.

[4] Dowling JA, Sun J, Pichler P, Rivest-Hénault D, Ghose S, Richardson H, et al. Automatic substitute computed tomography generation and contouring for magnetic resonance imaging (MRI)-alone external beam radiation therapy from standard MRI sequences. Int J Radiat Oncol 2015;93:1144–53. https://doi.org/10.1016/j.ijrobp.2015.08.045.

[5] Kim J, Glide-Hurst C, Doemer A, Wen N, Movsas B, Chetty IJ. Implementation of a novel algorithm for generating synthetic CT images from magnetic resonance imaging data sets for prostate cancer radiation therapy. Int J Radiat Oncol 2015;91:39–47. https://doi.org/10.1016/j.ijrobp.2014.09.015.

[6] Korhonen J, Kapanen M, Keyriläinen J, Seppälä T, Tenhunen M. A dual model HU conversion from MRI intensity values within and outside of bone segment for MRI-based radiotherapy treatment planning of prostate cancer. Med Phys 2013;41:011704. https://doi.org/10.1118/1.4842575.

[7] Artaechevarria X, Munoz-Barrutia A, Ortiz-de-Solorzano C. Combination strategies in multi-atlas image segmentation: application to brain MR data. IEEE Trans Med Imaging 2009;28:1266–77. https://doi.org/10.1109/TMI.2009.2014372.

[8] Mcjury M, O'Neill A, Lawson M, Mcgrath C, Grey A, Page W, et al. Assessing the image quality of pelvic MR images acquired with a flat couch for radiotherapy treatment planning. Br J Radiol 2011;84:750–5. https://doi.org/10.1259/bjr/27295679.

[9] Schmidt MA, Payne GS. Radiotherapy planning using MRI. Phys Med Biol 2015;60:R323–61. https://doi.org/10.1088/0031-9155/60/22/R323.

[10] Tyagi N, Fontenla S, Zelefsky M, Chong-Ton M, Ostergren K, Shah N, et al. Clinical workflow for MR-only simulation and planning in prostate. Radiat Oncol 2017;12:119. https://doi.org/10.1186/s13014-017-0854-4.

[11] Vonken EPA, Schär M, Yu J, Bakker CJG, Stuber M. Direct in vitro comparison of six three-dimensional positive contrast methods for susceptibility marker imaging. J Magn Reson Imaging 2013;38:344–57. https://doi.org/10.1002/jmri.23976.

[12] Varma G, Clough RE, Acher P, Sénégas J, Dahnke H, Keevil SF, et al. Positive visualization of implanted devices with susceptibility gradient mapping using the original resolution. Magn Reson Med 2011;65:1483–90. https://doi.org/10.1002/mrm.22710.

[13] Varma G, Pedersen SF, Taupitz M, Botnar RM, Dahnke H, Keevil SF, et al. Utilizing different methods for visualizing susceptibility from a single multi-gradient echo dataset. Magn. Reson. Mater. Phys., Biol. Med. 2009;22:297–308. https://doi.org/10.1007/s10334-009-0180-4.

[14] Delangre S, Vuong QL, Po C, Gallez B, Gossuin Y. Improvement of the off-resonance saturation, an MRI sequence for positive contrast with SPM particles: theoretical and experimental study. J Magn Reson 2016;265:99–107. https://doi.org/10.1016/j.jmr.2016.02.002.

[15] Dong Y, Chang Z, Xie G, Whitehead G, Ji JX. Susceptibility-based positive contrast MRI of brachytherapy seeds. Magn Reson Med 2015;74:716–26. https://doi.org/10.1002/mrm.25453.

[16] Ghose S, Mitra J, Rivest-Hénault D, Fazlollahi A, Stanwell P, Pichler P, et al. MRI-alone radiation therapy planning for prostate cancer: automatic fiducial marker detection. Med Phys 2016;43:2218–28. https://doi.org/10.1118/1.4944871.

[17] Maspero M, van den Berg CAT, Zijlstra F, Sikkes GG, de Boer HCJ, Meijer GJ, et al. Evaluation of an automatic MR-based gold fiducial marker localisation method for MR-only prostate radiotherapy. Phys Med Biol 2017;62:7981–8002. https://doi.org/10.1088/1361-6560/aa875f.

[18] Zijlstra F, Moerland MA, van der Voort van Zyp JRN, Noteboom JL, Viergever MA, Seevinck PR. Challenges in MR-only seed localization for postimplant dosimetry in permanent prostate brachytherapy. Med Phys 2017;44:5051–60. doi:https://doi.org/10.1002/mp.12505.

[19] Dinis Fernandes C, Dinh CV, Steggerda MJ, ter Beek LC, Smolic M, van Buuren LD, et al. Prostate fiducial marker detection with the use of multi-parametric magnetic resonance imaging. Phys Imaging Radiat Oncol 2017;1:14–20. https://doi.org/10.1016/j.phro.2017.02.001.

[20] Seevinck PR, de Leeuw H, Bos C, Bakker CJG. Highly localized positive contrast of small paramagnetic objects using 3D center-out radial sampling with off-resonance reception. Magn Reson Med 2011;65:146–56. https://doi.org/10.1002/mrm.22594.

[21] De Leeuw H, Seevinck PR, Bakker CJG. Center-out radial sampling with off-resonant reconstruction for efficient and accurate localization of punctate and elongated paramagnetic structures. Magn Reson Med 2013;69:1611–22. https://doi.org/10.1002/mrm.24416.

[22] de Leeuw H, M a Moerland, van Vulpen M, Seevinck PR, Bakker CJG. A dual-plane co-RASOR technique for accurate and rapid tracking and position verification of an Ir-192 source for single fraction HDR brachytherapy. Phys Med Biol 2013;58:7829–39. https://doi.org/10.1088/0031-9155/58/21/7829.

[23] Fessler JA, Sutton BP. Nonuniform fast Fourier transforms using min-max interpolation. IEEE Trans. Signal Process. 2003;51:560–74. https://doi.org/10.1109/TSP.2002.807005.

[24] Jonsson JH, Garpebring A, Karlsson MG, Nyholm T. Internal fiducial markers and susceptibility effects in MRI—simulation and measurement of spatial accuracy. Int J Radiat Oncol 2012;82:1612–8. https://doi.org/10.1016/j.ijrobp.2011.01.046.

[25] McNabb E, Wong R, Noseworthy MD. Resolution and registration in dual-plane co-RASOR MR. Phys Med Biol 2018;63:215005https://doi.org/10.1088/1361-6560/aae4d5.

[26] Dietrich O, Raya JG, Reeder SB, Reiser MF, Schoenberg SO. Measurement of signal-to-noise ratios in MR images: influence of multichannel coils, parallel imaging, and reconstruction filters. J Magn Reson Imaging 2007;26:375–85. https://doi.org/10.1002/jmri.20969.

[27] McNabb E, Wong R, Noseworthy MD. Localizing implanted fiducial markers using undersampled co-RASOR MR imaging. Magn Reson Imaging 2018;48:1–9. https://doi.org/10.1016/j.mri.2017.12.009.

[28] Schenck JF. The role of magnetic susceptibility in magnetic resonance imaging: MRI magnetic compatibility of the first and second kinds. Med Phys 1996;23:815–50. https://doi.org/10.1118/1.597854.

[29] Scheffler K, Lehnhardt S. Principles and applications of balanced SSFP techniques. Eur Radiol 2003;13:2409–18. https://doi.org/10.1007/s00330-003-1957-x.